RSC Advances

PAPER

View Article Online
View Journal | View Issue

Cite this: *RSC Adv.*, 2020, **10**, 42953

Received 4th June 2020
Accepted 13th November 2020

DOI: 10.1039/d0ra04937a

rsc.li/rsc-advances

Interzeolite conversion of a micronsized FAU to a nanosized CHA zeolite free of organic structure directing agent with a high CO_2 capacity†

Kristoffer H. Møller,[ab] Maxime Debost,[b] Louwanda Lakiss,[b] Søren Kegnæs*[a] and Svetlana Mintova*[b]

The interzeolite transformation of a micronsized FAU zeolite to a nanosized CHA zeolite *via* alkali treatment is presented. The impact of the selection of the FAU zeolite starting material on the properties of the produced CHA zeolite was analyzed by XRD, ICP, SEM, TEM, N_2 and CO_2 adsorption, and *in situ* FT-IR. The analysis showed that the choice of starting FAU zeolite had a large impact on the chemical composition, size, morphology, and porosity of the produced CHA zeolite. The as prepared CHA samples show high capacity toward CO_2 (4.26 mmol g^{-1}) and it was demonstrated that the chemisorbed *vs.* physisorbed CO_2 was controlled by varying the amount of alkali cations in the CHA zeolite.

Introduction

Zeolites are unique ordered microporous aluminosilicates which have found many uses in the chemical industry.[1] Zeolites have pores, and cages of molecular dimensions and can be used for molecular sieving. Molecular sieving is a very useful property in both catalysis[2–6] and molecules separation in gas and liquid phases.[7–9] With more than 240 [10] different zeolite framework structures, a key parameter is finding the zeolite structure that fits the right needs for the desired application. One zeolite structure that has received much attention lately is the small pore chabazite (CHA).[11–16] The chabazite zeolite consists of double six ring (d6r) rings and cha composite building units (cages). The cha composite building units are connected through 8 ring openings making the channels of about 3.8 Å that run in three dimensions.[17] One of the applications where the chabazite zeolite has shown to be useful is in the automotive industry where it acts as a catalyst support for the selective catalytic reduction (SCR) reaction in diesel vehicles due to its high stability and activity.[14,18–20] Other studies have shown that chabazite can be useful in gas adsorption and separation, where it can be used for natural gas or flue gas purification and for carbon capture due to the size selectivity for gasses.[7,21,22]

Chabazite can be synthesized using organic structure directing agents (OSDAs) which are typically costly and require calcination of the zeolite to remove the organic template.[23–27] Another way to obtain the CHA zeolite is through interzeolite transformation where only inorganic structure directing agents are used.[13,28–31] CHA obtained by an interzeolite transformation of faujasite (FAU) has been reported, however, only limited research has been dedicated on the effect of the starting material on the size and morphology of the final CHA crystals.

In the application of zeolites, mass transfer and diffusion of molecules through zeolite channels are very important and size of both zeolite crystals and pores have an effect on the utilization of the zeolite.[32] Higher utilization of the zeolite can be accomplished by introducing an additional porosity in the zeolite or by decreasing the size to reduce the mean diffusion path-length for molecules.[33–35]

Herein, we present the successful interzeolite transformation of micronsized FAU zeolite to nanosized CHA zeolite *via* alkali treatment. The composition, size, morphology, and adsorption characteristics of the produced nanosized CHA zeolites made from different FAU zeolites were studied and showed that the starting FAU zeolite has a large impact on the size, composition, and morphology of the final CHA zeolite product.

Experimental

Materials

Commercially available chemical were used as received. NaOH (99%, VWR chemicals), KOH (90%, flakes, Sigma Aldrich), water (double distilled), FAU(2.6) (CBV400, Zeolyst) zeolite, FAU(15) (CBV720, Zeolyst) zeolite, H_3BO_3 (99.8%, Sigma Aldrich), HF (40%, Fisher chemical), HCl (37%, VWR), HNO_3 (65%, Carlo Erba) CO_2 (99.9999, Air Liquide), CO (99.9999, Air Liquide).

Synthesis

Synthesis of CHA from low silica FAU. The synthesis of CHA from FAU(2.6) zeolite is based on the procedure reported by

---

[a] *Technical University of Denmark, Department of Chemistry, Kemitorvet 207, 2800 Kongens Lyngby, Denmark. E-mail: skk@kemi.dtu.dk*

[b] *ENSICAEN, Laboratoire Catalyse & Spectrochimie, 6 Boulevard Maréchal Juin, 14050 Caen Cedex 4, France. E-mail: svetlana.mintova@ensicaen.fr*

† Electronic supplementary information (ESI) available. See DOI: 10.1039/d0ra04937a

Bourgogne *et al.*[36] with modifications to the synthesis composition. NaOH (40 wt% in water), KOH (45 wt% in water), and water were mixed in a polypropylene container (PP, Nalgene) before FAU(2.6) was added to the container. The mixture was shaken for 30 s before it was put in a preheated oven at 95 °C under static conditions. After heating, the solid was isolated by centrifugation (20 000 rpm, 20 min), washed with water until neutral pH of the wash water, and dried at 50 °C overnight. See Table S1 in ESI† for details on amounts.

Synthesis of CHA from high silica FAU. Synthesis of CHA from FAU(15) zeolite was performed following the procedure described above. KOH (45 wt% in H_2O) was mixed with water in a PP container before the FAU(15) was added to the container. The mixture was shaken for 30 s before it was put in a preheated oven at 95 °C under static conditions. The solids were isolated by centrifugation (20 000 rpm for 20 min). The solid were washed with water by first dispersing the solid in 90 °C water followed by sonicated for 20 min and isolation by centrifugation (20 000 rpm, 20 min). The washing procedure was repeated until neutral pH of the wash water. The solid was dried at 50 °C overnight. See Table S1 in ESI† for details on amounts.

Characterization

X-ray powder diffraction was performed using a PANalytical X'Pert Pro diffractometer with CuKα monochromatized radiation ($\lambda = 1.5418$ Å). Nitrogen physisorption was performed on a Micromeretics 3 flex at liquid nitrogen temperature (77 K). The samples were degassed at 350 °C under vacuum prior to analysis. The surface area was determined by the Brunauer–Emmett–Teller (BET) method and micropore volume by the *t*-plot method. The total pore volume was determined from a single point at $P/P_0 = 0.97$ on the adsorption branch. CO_2 adsorption was performed on a Micromeretics ASAP 2020 at 273.15 K. The sample was degassed at 350 °C under vacuum prior to analysis. Scanning electron microscopy (SEM) was performed using a MIRA-LMH (TESCAN) fitted with a field emission gun using an accelerating voltage of 30.0 kV. The samples were dispersed on carbon tape and coated with Pt and Pd prior to analysis. Transmission electron microscopy (TEM) was performed on a FEI Tecnai T20 G2 microscope operating at 200 kV. The samples were dispersed on lacey carbon grid prior to analysis. Inductively Coupled Plasma Atomic Emission Spectrometry (ICP-AES) was performed using a Varian ICP-OES 720-ES instrument. 50 mg of solid samples was dissolved in 0.5 mL aqua regia and 3 mL HF at 110 °C for 1 h in a PTFE beaker and cooled to rt. After that, boric acid (1.8 g) was added to the beaker along with 96.5 g of water and shaken overnight for homogenization. *In situ* infrared spectroscopy with CO_2 as probe molecule was performed using a Nicolet 6700 IR spectrometer (Thermo Scientific, Villebon sur Yvette, France) equipped with a mercury cadmium telluride (MCT) detector and an extended KBr beam splitter. The spectra were recorded with 128 scans and a resolution of 4 cm^{-1}. For analysis, the solid was pressed as a self-supported wafer (about 20 mg for a disc of 2.01 cm^2). Prior to CO_2 adsorption, the solid was activated by heating the pellet at 350 °C for 2 h with a 3 h heating ramp under vacuum ($\sim 10^{-5}$ torr) which was then allowed to cool to room temperature. A spectrum with the activated pellet was used as a background and subtracted from the obtained spectra recorded at different concentrations of CO_2.

Additionally, *in situ* IR spectroscopy study using CO as a probe molecule was performed; the sample was activated at 350 °C for 2 h under vacuum ($\sim 10^{-5}$ torr). The IR spectra under CO delivery were recorded at 77 K.

Results and discussion

Materials and characterization

Interzeolite transformation of micronsized FAU zeolites with an initial Si/Al ratios of 15 (FAU(15)) and 2.6 (FAU(2.6)) to CHA was performed under treatment at 95 °C for 4–7 days in solution with the following chemical composition: vSi/xK/yNa/$z$$H_2O$ ratio of $v = 1$, $x = 0.76$–1, $y = 0$–0.25, $z = 30$–40. The preparation of nanosized CHA zeolites is based on a modified version reported by Bourgogne *et al.*[36] using a purely inorganic synthesis approach.

In general, the choice of reactions conditions, silica/alumina source and Si/Al ratio strongly affects the size and morphology of resulting crystal.[37] In this study, the Si/Al ratio of FAU (2.6 to 15 from Zeolyst) and the concentration of cations are varied to study the effect on the physicochemical properties of formed nanosized CHA materials under mild conditions (95 °C). In comparison, J. Kim and D. H. Kim previously produced CHA crystals of 300–500 nm by an interzeolite transformation of FAU (from Zeolyst) with Si/Al ratio of 6 at 140 °C.[39] Moreover from previous studies on interzeolite transformation of FAU to CHA *via* an OSDA-free synthesis it has been only successfully shown for FAU with a Si/Al = 6 or below, while studies using higher Si/Al ratio FAU are reported only *via* synthesis with OSDA and higher temperature.[31] T. Takata *et al.* has previously shown that it is possible to form nanosized CHA crystals from FAU with Si/Al = 15 and higher in the presence of a OSDA.[37] Our study is exclusively focusing on the OSDA-free synthesis. Details of selected experiments are presented in Table S1, ESI.†

X-ray powder diffraction

The X-ray powder diffraction (XRPD) patterns for the starting materials FAU(15) and FAU(2.6) are shown in Fig. 1. The XRPD patterns of corresponding products (CHA(2.3) and CHA(1.9)) after 7 and 4 days interzeolite transformations, respectively, are also shown in Fig. 1. The diffraction patterns clearly show intensive peaks corresponding to the CHA type framework structure. Fig. 1 clearly indicate successful interzeolite transformations since no traces of FAU zeolite are observed. A minor impurity peak likely corresponding to GME type zeolite in sample CHA(1.9) is observed (Fig. 1D). The presence of GME peak and the combination of broad and narrow peaks indicates the presence of stacking fault in CHA(1.9) as described in literature.[38,39] For CHA(2.3) there is no GME peak, however, there is a combination of broad and narrow peaks, which could indicate minor faulting or direction oriented growth.

Interzeolite transformation of micronsized FAU(15) to CHA (Table S1, entry 4†) results in CHA with a Si/Al ratio of 2.3

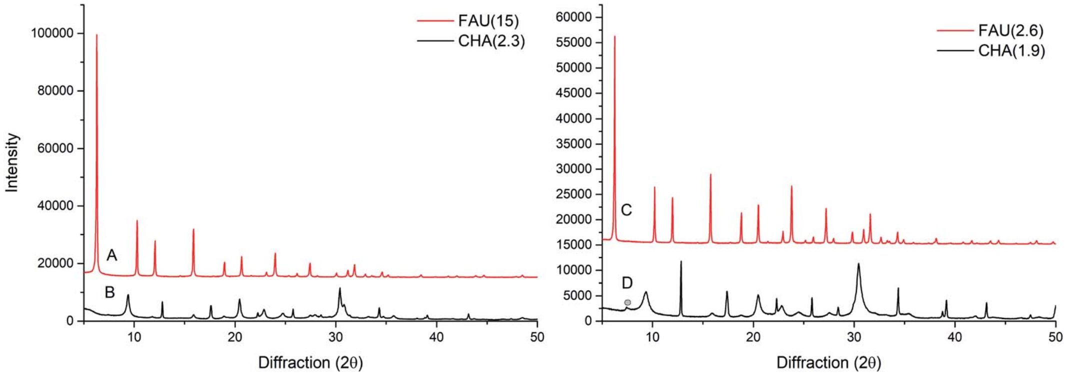

Fig. 1 XRPD patterns of (A) FAU(15), (B) CHA(2.3), (C) FAU(2.6), and (D) CHA(1.9); trace of impurity marked with circle.

(CHA(2.3)), whereas the interzeolite transformation of low silica FAU(2.6) (Table S1, entry 1†) results in CHA with a Si/Al ratio of 1.9. During this interzeolite transformation, only a part of the Si is retained in the CHA product from the starting FAU, however, the Si/Al of the starting materials has an influence on the chemical composition of the product. As evidenced, a higher Si/Al ratio in the starting FAU material results in a higher Si/Al in the product CHA. Considering the relative amount of Si going into the CHA zeolite, less of the initial Si is retained in the CHA(2.3) from FAU(15) compared to CHA(1.9) from FAU(2.6). The remaining Si is likely present as unreacted species in the reaction medium, lowering the yield of the zeolite. The difference in composition between samples CHA(2.3) and CHA(1.9) could potentially affect the application of the materials, since a higher Si/Al normally results in a higher thermal stability,[40] whereas a lower Si/Al has shown a stronger effect in selectivity for different gasses.[22]

Electron microscopy

The size and morphology of the zeolites were assessed by scanning electron microscopy (SEM) and transmission electron microscopy (TEM). The SEM image of FAU(15) (Fig. S1A†) shows that it consists of zeolite crystals of varying sizes (200–1000 nm) with a little rough surface. After interzeolite transformation to the product CHA(2.3) the crystals appearance changed. CHA(2.3) consists of agglomerates (~500 nm in size) of smaller zeolite crystals of 50–100 nm (Fig. S1B and S2†). The shaped of the agglomerated indicates some oriented growth of the nanosized crystallites. The mechanism for interzeolite transformation has been suggested to proceed through a dissolution of the zeolite crystals that breaks up into smaller building units which then are used to construct new zeolite form.[41–44] These nanoparts are then directed by the K^+ to form CHA rather than other zeolite structures which are directed by different cations, as described by van Tendeloo *et al.*[30] It is speculated if this is the case and that the mesopores in the FAU(15) could facilitate a dissolution of the crystal into smaller crystals which would result in the formation of smaller CHA zeolite crystals. It is unknown whether the zeolites dissolves and recrystallize in the solution or on the surface of the dissolving FAU zeolites. For the interzeolite transformation of FAU(2.6), the parent zeolite consists of both larger zeolite crystals of 200–1000 nm but also has smaller crystals of 100–150 nm (Fig. S1C†). Based on SEM analysis, the CHA(1.9) crystals compared to CHA(2.3) is much different (Fig. S1D and S3†). The CHA(1.9) zeolite contains more plate/disc-like structured particles consisting of smaller zeolite crystals with its rough looking surface, however, it is not possible to see individual small zeolite crystals making up the plate. It is possible that the presence of small FAU crystals in the FAU(2.6) zeolite aids the synthesis of smaller plate-like CHA zeolite crystals. The plate-like morphology is a typical shape of faulted CHA, which is consistent with the observations in the XRD pattern.[39] For both CHA(1.9) and CHA(2.3) there is some oriented growth of the zeolite. It is speculated if this could arise from faulting, when purely inorganic SDAs are used rather than when OSDAs are used for synthesis.

Fig. 2 shows the TEM images of both CHA(1.9) and CHA(2.3) samples. The CHA(1.9) contains crystals with a size of 300–500 nm (Fig. 2A) consisting of densely packed smaller crystallites. Fig. S4† shows lower magnification TEM images of CHA(1.9) which indicates the plate-like morphology with smaller crystallites growing from the plate. This is consistent with the SEM observations made for the CHA(1.9) sample. The CHA(2.3) sample contains very small crystallites in discrete form (Fig. 2B). The size of the individual zeolite crystals is about 50 nm, and the crystalline fringes are clearly observed in the TEM images. Fig. S5† shows TEM images of agglomerates of CHA(2.3). Here, it appears that smaller zeolite crystals are overlapping, which is consistent with the agglomerates

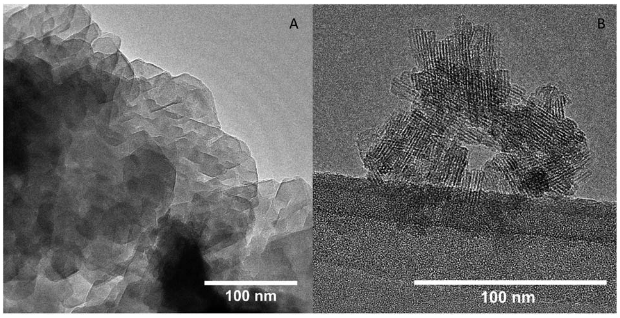

Fig. 2 TEM images of samples CHA(1.9) (A) and CHA(2.3) (B).

observed in SEM, however, it is difficult to see any direction oriented growth. The Si/Al ratio of the starting FAU materials and the concentration of both cations and hydroxide are different for the synthesis of two CHA zeolites. Those are the main factors that affect the morphology and the size of the final product. Based on those two samples the larger Si/Al ratio in FAU results in the smallest crystal size (FAU(15) to CHA(2.3) gives crystals of 50–100 nm). This correspond well with the previous studies where Si/Al = 15 and higher (and using a OSDA at 125–170 °C) also results in nanosized crystals.[37] However, J. Kim and D. H. Kim[39] showed a Si/Al = 6 (OSDA-free at 140 °C) results in larger crystal size similar to the once obtained here for CHA(1.9) produced from FAU(2.6). By studying different Si/Al ratios and silica/alumina sources, T. Takata concluded that the starting reaction mixture with common composite building unit and suitable Si/Al ratio causes abundant and uniform nucleation, resulting in the formation of nanosized CHA zeolites.[37]

Porosity and CO_2 capacity

The porosity of CHA(2.3) and CHA(1.9) zeolite samples was assessed by nitrogen physisorption measurements. The N_2 physisorption isotherm of FAU(2.6), FAU(15), CHA(1.9), and CHA(2.3) are shown in Fig. S6–S9.† The N_2 isotherm for CHA(2.3) reveals the presence of both micro- and mesoporosity from the uptake at low pressure (<0.01 P/P_0) and from the uptake of N_2 at higher pressure, respectively (Fig. S9†). The calculated porosity for FAU and CHA zeolites are listed in Table S3.† CHA(2.3) exhibits a high BET surface area of 251 $m^2\ g^{-1}$ compared to other CHA zeolites in the K-form obtained from interzeolite conversion.[45–47] The total pore volume of 0.39 $cm^3\ g^{-1}$ has only a limited contribution from the micropores with 0.04 $cm^3\ g^{-1}$, hence the total porosity of the material is primarily mesopores. The hysteresis loop at high P/P_0 for nanosized CHA(2.3) is due the presence of textural (interparticle) porosity, which is typical for nanosized zeolites.[34] On the other hand CHA(1.9) has significantly lower surface area of 43 $m^2\ g^{-1}$ and a total pore volume of 0.07 $cm^3\ g^{-1}$ of which 0.004 $cm^3\ g^{-1}$ is the micropore volume. This is typically seen for the K form of the CHA zeolite obtained from the transformation in the potassium form.[45–47] CHA(1.9) is almost exclusively in the K form determined by ICP analysis (93% K and 6% Na relative to Al) which is the reason for this low porosity. It's reported that the K^+ extra-framework cations sit in the channels of CHA with low Si/Al ratio and limits the access of N_2 to the channels, thus, lowering the surface area determined by N_2 physisorption at 77 K.[12,45] CHA(1.9) does not show the same interparticle porosity which suggest that smaller crystals are grown together and are not accessible for the N_2 molecules at 77 K. Considering the higher micropore volume for CHA(2.3) compared to CHA(1.9), it could be a result of the higher mesoporosity which provides access to more pore mouth openings of the CHA zeolite. The interparticle mesoporosity of CHA(2.3) and the lack of this in CHA(1.9) is consistent with the SEM and TEM observations for the two samples. This illustrates the large effect that the starting zeolite has on the porosity of the obtained CHA with the agglomerates of discrete nanosized CHA zeolite crystals (CHA(2.3)) rather than the thin plates of intergrown CHA zeolite (CHA(1.9)). Changing the cation in CHA greatly affects the adsorption properties of CHA. This was nicely demonstrated by Shang *et al.*,[12] who showed that changing to a smaller cation than K^+ increases the uptake of N_2. However, both Si/Al, type of cation and degree of ion-exchange affects the adsorption properties of CHA.

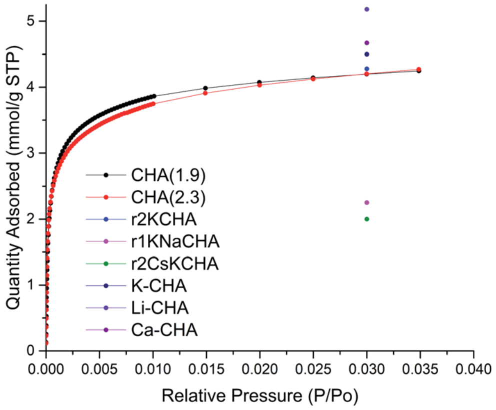

Fig. 3 CO_2 adsorption of samples CHA(2.3) (red) and CHA(1.9) (black) at 273.15 K. CO_2 capacity from Zhang *et al.*[7] (K-CHA, Li-CHA, and Ca-CHA) and Shang *et al.*[12] (r1KNaCHA, r2KCHA, and r2CsKCHA) reported as single points at relative pressure of 0.030 (104 kPa).

One of the applications of CHA is the selective capture of CO_2 [7,21,22] hence, the capacity of CO_2 was measured to evaluate the potential use of the newly synthesized materials. The accessibility of CO_2 and not N_2 in the K-CHA zeolite has been shown before and this is related to the different polarizability of the two gas molecules with CO_2 being much more polarizable.[45] CHA(2.3) shows a large uptake of CO_2 at low relative pressure and then levels off at higher relative pressure (Fig. 3). Interestingly, the difference of the two CHA zeolites with either interparticle porosity (CHA(2.3)) or intergrown CHA (CHA(1.9)) does not have a large impact on the adsorption profile and capacity of CO_2. At $P/P_0 = 0.030$, the CO_2 capacity of CHA(2.3) is 4.26 mmol g^{-1}, which is similar to the CHA(1.9) of 4.25 mmol g^{-1}. The CO_2 capacity is close to other similar reported materials[7,12] (see reference points in Fig. 3), however, it is hard to make a profound comparison, since both Si/Al ratio together with the location of cations affect the capacity. Additionally, the amount and location of cations also affect the selectivity of CHA zeolite for different gasses.[7]

FT-IR

CO_2 adsorption. The CO_2 adsorption on the CHA zeolites was studied by *in situ* FTIR (Fig. 4 and S10–S13†). Two modes of CO_2 adsorption, *i.e.*, physisorbed CO_2 at 2348 cm^{-1},[48] and the chemisorbed CO_2 giving rise to carbonates such as mono, bi, polydentate carbonates are measured.[21,49–51] The nature of the formed carbonates depends on the zeolite type structure and the polarizing effect of the compensating cations present in the porosity.[52] The IR spectra of the activated samples before CO_2

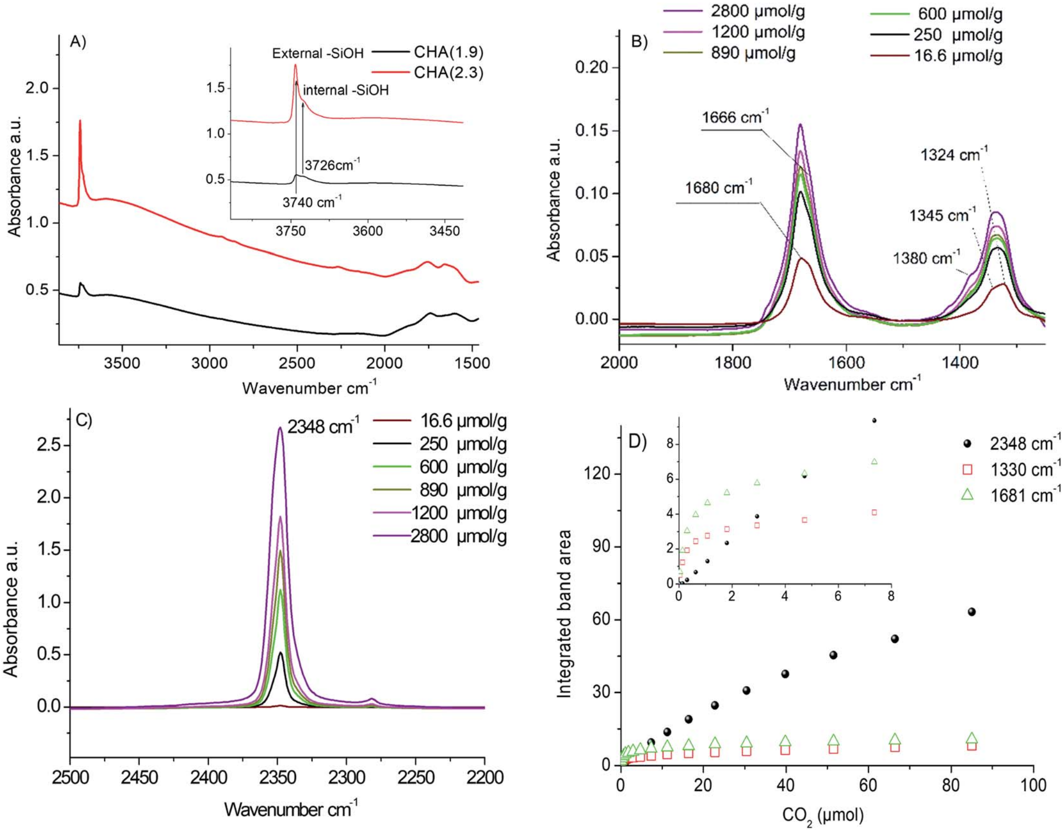

Fig. 4 IR spectra of CHA(1.9) and CHA(2.3) after activation at 350 °C under vacuum in the region 1500–4000 cm^{-1}; the spectra were normalized to 20 mg (A). IR spectra under pulsed CO_2 adsorption on CHA(2.3) in the regions of 2000–1250 cm^{-1} (B), 2500–2200 cm^{-1} (C) and integrated area of bands in FTIR spectra corresponding to chemisorbed CO_2 at 1330 cm^{-1} and 1681 cm^{-1} and physisorbed CO_2 at 2348 cm^{-1} (D).

adsorption reveal two distinct bands in the OH region (Fig. 4A). The first band at 3740 cm^{-1} is assigned to external terminal silanol sites, while the band at 3726 cm^{-1} is attributed to internal silanol nests or silanol defects.[53] As shown in Fig. 4A, CHA(2.3) displays a higher amount of silanol sites, both external and internal silanol sites. The height ratio of the external silanol band at 3740 cm^{-1}, between the two samples after normalization to the weight of the pellet is equal to 6. This implies that sample CHA(2.3) displays an external surface area 6 times higher than sample CHA(1.9). The ratio is in reasonable agreement with external surface area ratio obtained from the N_2 physisorption measurements which is 4.9. This is mainly due to the formation of nanosized crystals that are improving the adsorption of nitrogen. CHA(2.3) has also a higher amount of internal silanol sites as confirmed by the high intensity of the band at 3726 cm^{-1} (the ratio is 2.6). This result is in a good agreement with the nitrogen sorption analyses that showed structured mesoporosity for sample CHA(2.3).

Fig. 4B and C reports the difference spectra obtained at adsorption of a specific dose of CO_2 after subtraction of the background (the IR spectrum recorded after activation of the samples). After the first CO_2 dose delivered, two broad bands are observed at 1324 cm^{-1} and 1680 cm^{-1}. After several doses, two additional distinct bands at 1665 cm^{-1} and 1345 cm^{-1} appeared. The bands at 1324 cm^{-1} and 1680 cm^{-1} are attributed to carbonate species formed during CO_2 adsorption (Fig. 4B). As shown in Fig. 4D, these bands increase by increasing CO_2 doses to reach saturation at 40–60 μmol g^{-1} CO_2 (~1 μmol CO_2 for 20 mg sample). It is already reported in the literature that the double degenerated ν_3 vibration of the carbonates is usually split into two bands.[54] Busca *et al.*[55] used the shift between these two bands to identify the carbonate species. In our case, the $\Delta\nu_3$ for 1680–1324 cm^{-1} and 1665–1354 cm^{-1} is higher than 300 cm^{-1}, which corresponds to bidentate carbonates. Such a result is in a good agreement with the low Si/Al ratio of the samples, which gives rise to strong basic zeolite sites. In addition, a new band assigned to physisorbed CO_2 appears at 2348 cm^{-1} due to the polarization of CO_2 by the compensating cations present in the CHA crystals.[48] The intensity of the band at 2348 cm^{-1} increases with an increase of the CO_2 pressure (Fig. 4C). Moreover, a new shoulder at 1380 cm^{-1} appeared. This shoulder is also attributed to physisorbed CO_2 molecules.[48] At high loading, more than 3000 μmol g^{-1} of CO_2, a shift of the silanol bands at 3740–3725 cm^{-1} is observed, which is due to the perturbation of silanol sites by CO_2 molecules (see Fig. S10†).

The evolution of the integrated band area of the carbonates at 1325 cm^{-1} and 1681 cm^{-1} and the polarized CO_2 at 2348 cm^{-1} as a function of the amount of CO_2 introduced in the cell is depicted in Fig. 4D. Three distinct phenomena are observed (i) first at a low CO_2 loading, CO_2 is interacting with strong basic sites of zeolite leading to the formation of carbonates. This is traduced by the rising of the bands in the region 1300–1400 cm^{-1} and 1600–1700 cm^{-1}; (ii) after introduction of 4–5 μmol of CO_2, the strongest basic sites of zeolite are completely neutralized with carbonates. No more carbonates are formed; the IR bands at 1325 cm^{-1} and 1681 cm^{-1} corresponding to carbonates reached saturation that correspond to 200 μmol CO_2 per g of zeolite. Only the band at 2348 cm^{-1} related to the interaction of CO_2 with the extra-framework cations continues to increase linearly with the amount of CO_2 introduced; (iii) at a higher amount of CO_2, above 3500–4000 μmol g^{-1} of zeolite, after a complete consumption of the cationic sites, a shift of the silanol bands in the region 3700–3750 cm^{-1} is observed. This is due to the perturbation of the external silanol sites by CO_2. This amount is in a good agreement with the amount of extra-framework cations as determined by ICP (about 3600 μmol of potassium per g of zeolite).

The amount of carbonates formed on the two samples is estimated based on the integrated areas of the bands at 1325 cm^{-1} and 1681 cm^{-1}. Since the absorption coefficient is unknown, we calculated the height ratio of the two bands (A_{1325} CHA(1.9)/A_{1325} CHA(2.3) = 1.56 and A_{1681} CHA(1.9)/A_{1681} CHA(2.3) = 1.6). This means that the amount of strong basic sites of CHA(1.9) compared to CHA(2.3) is 1.6 times higher. For physisorbed species, the integrated band area is almost the same for the two samples with a ratio equal to 0.9.

The desorption properties of CHA(2.3) was tested by desorption of CO_2 until a pressure of 10^{-5} torr. Fig. S14† shows the IR bands for the chemisorbed and physisorbed species at 2800 μmol g^{-1} and at 10^{-5} torr. This clearly shows that the physisorbed species are absent after desorption whereas the chemisorbed species are much more strongly bound at present and still are present at 10^{-5} torr in similar quantities. Thus, the physisorbed species can reversibly be adsorbed and desorbed to CHA(2.3). A similar trend is observed for CHA(1.9) (not shown).

CO adsorption. To further investigate the type and strength of interaction between adsorbates and cationic sites, CO adsorption was performed on CHA(1.9). The CO probe molecule is commonly used to distinguish between the different cationic sites present in zeolites. CO molecule is very sensitive to its environment and can easily reveal the types of cationic sites located in different confined space.[56–58] The experiment was performed with pulses of CO at 77 K and monitored by *in situ* IR. The IR spectra recorded at different doses of CO delivered to the sample are shown in Fig. S14.† Two main IR absorption bands at 2147 cm^{-1} and 2160 cm^{-1} are observed. These bands arise from the polarization of CO by cationic sites, in our case the potassium present in the CHA zeolite.[56–58] This leads to a blue shift of the fundamental CO vibrational mode as compared to the band at 2143 cm^{-1} corresponding to free CO molecules. Thus, the IR absorption band at 2160 cm^{-1} corresponds to strong cationic acid sites of CHA zeolite. Indeed, the band at 2147 cm^{-1} might result from the interaction of CO with potassium cations located in a more confined space. In this case, the positive electric field of potassium cations are highly perturbed and weakened by neighbouring negative oxygen atoms.

Conclusions

The morphology, size and porosity of the CHA zeolite was found to be highly dependent by the type of the initial FAU zeolite samples. Using appropriate conditions, the transformation from two FAU-type zeolites to CHA-type zeolites was accomplished by alkali treatment without the use of an organic structure directing agent. The CHA(2.3) sample consisted of 50–100 nm discrete zeolite crystals while the CHA(1.9) sample consisted of big agglomerated crystals. Both zeolite samples CHA(1.9) and CHA(2.3) showed an extremely high CO_2 adsorption capacity. The amount of chemisorbed CO_2 species on the CHA zeolite is strongly related to the Si/Al ratio of the material. The sample CHA(1.9) with low Si/Al ratio showed higher amount of carbonate species which is proportional to the amount of compensating cations in zeolite structure.

Conflicts of interest

There are no conflicts to declare.

Acknowledgements

Dr Farnoosh Goodarzi is thanked for doing TEM analysis on the zeolites. Engineer Valérie Ruaux and Technician Marie Desmurs is thanked for their help with obtaining IR, ICP, N_2 physisorption and CO_2 adsorption data. The authors are grateful for funding from Haldor Topsøe A/S, Independent Research Fund Denmark (grant no. 6111-00237), and Villum fonden (grant no. 13158).

Notes and references

1 T. Maesen, in *Introduction to Zeolite Science and Practice*, ed. J. Čejka, H. van Bekkum, A. Corma and F. Schüth, Elsevier, Amsterdam, 2007, vol. 168, pp. 1–12.

2 C. Liu, J. Liu, S. Yang, C. Cao and W. Song, *ChemCatChem*, 2016, **8**, 1279–1282.

3 M. Choi, Z. Wu and E. Iglesia, *J. Am. Chem. Soc.*, 2010, **132**, 9129–9137.

4 D. Fraenkel, M. Cherniavsky, B. Ittah and M. Levy, *J. Catal.*, 1986, **101**, 273–283.

5 F. Goodarzi, R. P. Thumbayil, K. Enemark-Rasmussen, J. Mielby, T. T. M. Nguyen, P. Beato, F. Joensen and S. Kegnæs, *ChemCatChem*, 2020, **12**, 1519–1526.

6 F. Goodarzi, L. Kang, F. R. Wang, F. Joensen, S. Kegnæs and J. Mielby, *ChemCatChem*, 2018, **10**, 1566–1570.

7 J. Zhang, R. Singh and P. A. Webley, *Microporous Mesoporous Mater.*, 2008, **111**, 478–487.

8 Y. Zheng, N. Hu, H. Wang, N. Bu, F. Zhang and R. Zhou, *J. Membr. Sci.*, 2015, **475**, 303–310.

9 S. Imasaka, M. Itakura, K. Yano, S. Fujita, M. Okada, Y. Hasegawa, C. Abe, S. Araki and H. Yamamoto, *Sep. Purif. Technol.*, 2018, **199**, 298–303.

10 International Zeolite Association Structure Commission, *Database Zeolite Struct.*, 2017.

11 X. Li, H. Kita, H. Zhu, Z. Zhang, K. Tanaka and K. Okamoto, *Microporous Mesoporous Mater.*, 2011, **143**, 270–276.

12 J. Shang, G. Li, R. Singh, P. Xiao, J. Z. Liu and P. A. Webley, *J. Phys. Chem. C*, 2013, **117**, 12841–12847.

13 Y. Ji, M. A. Deimund, Y. Bhawe and M. E. Davis, *ACS Catal.*, 2015, **5**, 4456–4465.

14 J. H. Kwak, R. G. Tonkyn, D. H. Kim, J. Szanyi and C. H. F. Peden, *J. Catal.*, 2010, **275**, 187–190.

15 X. Wang, Q. Wu, C. Chen, S. Pan, W. Zhang, X. Meng, S. Maurer, M. Feyen, U. Müller and F. S. Xiao, *Chem. Commun.*, 2015, **51**, 16920–16923.

16 Y. Shan, X. Shi, J. Du, Z. Yan, Y. Yu and H. He, *Ind. Eng. Chem. Res.*, 2019, **58**, 5397–5403.

17 C. Baerlocher, L. B. McCusker and D. H. Olson, *Atlas of Zeolite Framework Types*, Elsevier, Amsterdam, 6th edn, 2007.

18 S. T. Korhonen, D. W. Fickel, R. F. Lobo, B. M. Weckhuysen and A. M. Beale, *Chem. Commun.*, 2011, **47**, 800–802.

19 J. H. Kwak, D. Tran, S. D. Burton, J. Szanyi, J. H. Lee and C. H. F. Peden, *J. Catal.*, 2012, **287**, 203–209.

20 D. W. Fickel and R. F. Lobo, *J. Phys. Chem. C*, 2010, **114**, 1633–1640.

21 T. D. Pham, Q. Liu and R. F. Lobo, *Langmuir*, 2013, **29**, 832–839.

22 J. Shang, G. Li, R. Singh, Q. Gu, K. M. Nairn, T. J. Bastow, N. Medhekar, C. M. Doherty, A. J. Hill, J. Z. Liu and P. A. Webley, *J. Am. Chem. Soc.*, 2012, **134**, 19246–19253.

23 M. Moliner, J. E. Gabay, C. E. Kliewer, R. T. Carr, J. Guzman, G. L. Casty, P. Serna and A. Corma, *J. Am. Chem. Soc.*, 2016, **138**, 15743–15750.

24 D. W. Fickel, E. D'Addio, J. A. Lauterbach and R. F. Lobo, *Appl. Catal., B*, 2011, **102**, 441–448.

25 U. Deka, A. Juhin, E. A. Eilertsen, H. Emerich, M. A. Green, S. T. Korhonen, B. M. Weckhuysen and A. M. Beale, *J. Phys. Chem. C*, 2012, **116**, 4809–4818.

26 M. Itakura, I. Goto, A. Takahashi, T. Fujitani, Y. Ide, M. Sadakane and T. Sano, *Microporous Mesoporous Mater.*, 2011, **144**, 91–96.

27 S. I. Zones, *US Pat.* US4544538, 1985.

28 S. Miyagawa, K. Miyake, Y. Hirota, N. Nishiyama, M. Miyamoto, Y. Oumi and S. Tanaka, *Microporous Mesoporous Mater.*, 2019, **278**, 219–224.

29 H. Robson and K. P. Lillerud, *Verified Syntheses of Zeolitic Materials*, Elsevier, Amsterdam, 2nd rev., 2001.

30 L. van Tendeloo, E. Gobechiya, E. Breynaert, J. A. Martens and C. E. A. Kirschhock, *Chem. Commun.*, 2013, **49**, 11737–11739.

31 M. Dusselier and M. E. Davis, *Chem. Rev.*, 2018, **118**, 5265–5329.

32 J. O. Abildstrøm, M. Kegnæs, G. Hytoft, J. Mielby and S. Kegnæs, *Microporous Mesoporous Mater.*, 2016, **225**, 232–237.

33 J. Pérez-Ramírez, C. H. Christensen, K. Egeblad, C. H. Christensen and J. C. Groen, *Chem. Soc. Rev.*, 2008, **37**, 2530–2542.

34 H. Awala, J.-P. Gilson, R. Retoux, P. Boullay, J.-M. Goupil, V. Valtchev and S. Mintova, *Nat. Mater.*, 2015, **14**, 447–451.

35 J. van den Bergh, J. Gascon and F. Kapteijn, in *Zeolites and Catalysis*, Wiley-VCH Verlag GmbH & Co. KGaA, Weinheim, Germany, 2010, vol. 1, pp. 361–387.

36 M. Bourgogne, J.-L. Guth and R. Way, *US Pat.* 4503024, 1985.

37 T. Takata, N. Tsunoji, Y. Takamitsu, M. Sadakane and T. Sano, *Microporous Mesoporous Mater.*, 2016, **225**, 524–533.

38 K. P. Lillerud, R. Szostak and A. Long, *J. Chem. Soc., Faraday Trans.*, 1994, **90**, 1547–1551.

39 J. Kim and D. H. Kim, *Microporous Mesoporous Mater.*, 2018, **256**, 266–274.

40 L. B. McCusker and C. Baerlocher, in *Introduction to Zeolite Science and Practice*, eds. J. Čejka, H. van Bekkum, A. Corma and F. Schüth, Elsevier, Amsterdam, 2007, vol. 168, pp. 13–37.

41 C. Li, M. Moliner and A. Corma, *Angew. Chem., Int. Ed.*, 2018, **57**, 15330–15353.

42 A. Yashiki, K. Honda, A. Fujimoto, S. Shibata, Y. Ide, M. Sadakane and T. Sano, *J. Cryst. Growth*, 2011, **325**, 96–100.

43 I. Goto, M. Itakura, S. Shibata, K. Honda, Y. Ide, M. Sadakane and T. Sano, *Microporous Mesoporous Mater.*, 2012, **158**, 117–122.

44 H. Jon, N. Ikawa, Y. Oumi and T. Sano, *Chem. Mater.*, 2008, **20**, 4135–4141.

45 F. N. Ridha, Y. Yang and P. A. Webley, *Microporous Mesoporous Mater.*, 2009, **117**, 497–507.

46 K. H. Rasmussen, J. Mielby and S. Kegnaes, *ChemCatChem*, 2018, **10**, 4380–4385.

47 R. Nedyalkova, C. Montreuil, C. Lambert and L. Olsson, *Top. Catal.*, 2013, **56**, 550–557.

48 A. Villarreal, P. Castillo-Villalón and J. Ramírez, *J. Mex. Chem. Soc.*, 2017, **61**, 102–108.

49 T. Montanari and G. Busca, *Vib. Spectrosc.*, 2008, **46**, 45–51.

50 E. Gallei and G. Stumpf, *J. Colloid Interface Sci.*, 1976, **55**, 415–420.

51 R. W. Stevens, R. V. Siriwardane and J. Logan, *Energy Fuels*, 2008, **22**, 3070–3079.

52 J. C. M. Pires, F. G. Martins, M. C. M. Alvim-Ferraz and M. Simões, *Chem. Eng. Res. Des.*, 2011, **89**, 1446–1460.

53 S. M. Maier, A. Jentys and J. A. Lercher, *J. Phys. Chem. C*, 2011, **115**, 8005–8013.

54 J. Fujita, A. E. Martell and K. Nakamoto, *J. Chem. Phys.*, 1962, **36**, 339–345.

55 G. Busca and V. Lorenzelli, *Mater. Chem.*, 1982, **7**, 89–126.

56 K. I. Hadjiivanov and G. N. Vayssilov, *Adv. Catal.*, 2002, **47**, 307–511.

57 A. Zecchina and C. O. Areán, *Chem. Soc. Rev.*, 1996, **25**, 187–197.

58 C. Lamberti, A. Zecchina, E. Groppo and S. Bordiga, *Chem. Soc. Rev.*, 2010, **39**, 4951–5001.